



HAL
open science

Robin-Robin loose coupling for incompressible fluid-structure interaction: non-linear setting and nearly-optimal error analysis

Erik Burman, Rebecca Durst, Miguel Angel Fernández, Johnny Guzmán,
Oscar Ruz

► To cite this version:

Erik Burman, Rebecca Durst, Miguel Angel Fernández, Johnny Guzmán, Oscar Ruz. Robin-Robin loose coupling for incompressible fluid-structure interaction: non-linear setting and nearly-optimal error analysis. 2023. hal-04258861v2

HAL Id: hal-04258861

<https://inria.hal.science/hal-04258861v2>

Preprint submitted on 27 Oct 2023

HAL is a multi-disciplinary open access archive for the deposit and dissemination of scientific research documents, whether they are published or not. The documents may come from teaching and research institutions in France or abroad, or from public or private research centers.

L'archive ouverte pluridisciplinaire **HAL**, est destinée au dépôt et à la diffusion de documents scientifiques de niveau recherche, publiés ou non, émanant des établissements d'enseignement et de recherche français ou étrangers, des laboratoires publics ou privés.



Distributed under a Creative Commons Attribution 4.0 International License

[10] that the Nitsche coupling method could be transformed into Robin type coupling scheme without loss of stability. Robin conditions had been shown to perform well as a preconditioner already in [1]. A number of studies have since then been reported in the literature on Robin-like loose coupling for incompressible FSI involving thick-walled solids (see, e.g., [2, 18, 5, 21, 22]), but without rigorous error analysis nor convergence rates. In [17], it is shown that the generalized Robin-Neumann scheme of [18] introduces a splitting error scaling as $\mathcal{O}(\tau/h^{\frac{1}{2}})$, which requires a $\tau \lesssim h^{\frac{3}{2}}$ condition for accuracy (not for stability).

In [10], the Robin coefficient inherited the $\mathcal{O}(h^{-1})$ scaling from Nitsche's method, but it was noted numerically that this scaling appeared not to be necessary for the stability of the algorithm. In a recent development [8], it was shown for a semi-discretization in time that the coupling scheme indeed is stable independent of the added mass effect and an error estimate of order $\mathcal{O}(\tau^{\frac{1}{2}})$, where τ denotes the time step, was shown. Another result in this spirit was reported in [27], for a fully discrete Robin-Robin method and under a CFL-like condition on the discretization parameters. A stability estimate for the time semi-discretized problem with moving fluid domain is also provided, but the treatment of the convective term involves an artificial modification of the fluid velocity on the interface. An alternative fully discrete formulation is introduced in [6], where the stresses are represented in terms of Lagrange multipliers or variational residuals, and the exponential growth of the stability factor was moderated to sub-linear growth without conditions on the discretization parameters. Finally, both for the cases of parabolic-parabolic and parabolic-hyperbolic couplings, it was shown in [7] that in most situations one can expect the nearly-optimal order $\mathcal{O}(\tau\sqrt{1+\log\tau^{-1}})$. Depending on the physical parameters however it was noted that this may not be attained, except for very small time steps unless the parameter in the Robin condition is chosen carefully.

The objective of the present paper is to build on the results of [6, 7] and extend them to more realistic settings, showing that the Robin-Robin loose coupling is indeed expected to result in a first order time discretization scheme also in physically relevant situations. The scientific contributions of this work are three fold. First, in a fully non-linear setting (coupling viscous incompressible flow in moving domains with the dynamics of an hyper-elastic solid), we provide a rigorous fully discrete formulation with suitable stabilization terms which guarantee unconditional energy stability. Second, in the linear case, we present the extension of the nearly-optimal error analysis from [7] to the case of the Stokes-elasticity system. To the best of our knowledge, this is the first time that such accuracy is proved for a loosely coupled scheme in incompressible fluid-structure interaction involving thick-walled solids. The latter results were first reported in [13, Chapter 5] and, therefore, the proofs are only sketched herein. Finally, the accuracy properties of the proposed method are illustrated in a series of well-known numerical examples. We in particular investigate the dependence of the accuracy on the physical parameters and the choice of the free parameter in the Robin coupling.

The rest of the paper is organized as follows. In Section 2, we introduce the considered physically realistic setting. We show how to extend the fully discrete formulation of [6] to this nonlinear case and prove the fundamental stability estimate in Section 3. Section 4 is devoted to the derivation of the nearly-optimal error estimate in a simplified linear setting. Finally, the paper is ended with some numerical examples which are reported in Section 5.

88 **2. Problem setting.** We consider a fluid-structure interaction system in which
 89 the fluid is modeled by the incompressible Navier-Stokes equations, in arbitrary
 90 Lagrangian-Eulerian (ALE) formalism, and the solid by the non-linear elastody-
 91 namics equations. The reference configuration of system is given by the domain
 92 $\Omega \stackrel{\text{def}}{=} \Omega^f \cup \Omega^s \subset \mathbb{R}^d$, with $d = 2, 3$. For all time $t > 0$, the current solid configuration
 93 is denoted by $\Omega^s(t) \subset \mathbb{R}^d$, whereas $\Omega^f(t) \subset \mathbb{R}^d$ stands for the moving fluid control
 94 volume. We denote by $\Sigma(t) \stackrel{\text{def}}{=} \partial\Omega^f(t) \cap \partial\Omega^s(t)$ the current configuration of the fluid-
 95 structure interface, whose reference configurations corresponds to $\Sigma \stackrel{\text{def}}{=} \partial\Omega^f \cap \partial\Omega^s$.
 96 The remaining parts of the fluid and solid boundaries are supposed to be time inde-
 97 pendent and partitioned as $\partial\Omega^f = \Gamma^f \cup \Sigma$ and $\partial\Omega^s = \Gamma^s \cup \Sigma$.

The moving fluid domain $\Omega^f(t)$ can be parametrized in terms of the so-called ALE
 map, $\mathcal{A} : \Omega^f \times \mathbb{R}^+ \rightarrow \mathbb{R}^d$, in such a way that $\Omega^f(t) = \mathcal{A}(\Omega^f, t)$. The ALE deformation
 map \mathcal{A} is often written in terms of fluid domain displacement $\mathbf{d}^f : \Omega^f \times \mathbb{R}^+ \rightarrow \mathbb{R}^d$ via
 the relation $\mathcal{A} = \mathbf{I}_{\Omega^f} + \mathbf{d}^f$, where \mathbf{I}_{Ω^f} stands for the identity operator in Ω^f . We can
 hence introduce the notation $\mathcal{A}_t \stackrel{\text{def}}{=} \mathcal{A}(\cdot, t)$, the fluid domain velocity $\mathbf{w} \stackrel{\text{def}}{=} \partial_t \mathcal{A} =$
 $\partial_t \mathbf{d}^f$, the fluid gradient of deformation $\mathbf{F} \stackrel{\text{def}}{=} \nabla \mathcal{A}$ (spatial gradient) and its Jacobian
 $J \stackrel{\text{def}}{=} \det \mathbf{F}$. For a given field f defined in the current configuration $\Omega^f(t)$, we shall
 use the notation \hat{f} to defined its corresponding ALE description in Ω^f , by composing
 with the ALE map, namely,

$$\hat{f}(\mathbf{x}, t) \stackrel{\text{def}}{=} f(\mathcal{A}(\mathbf{x}, t), t) \quad \forall \mathbf{x} \in \Omega^f.$$

98 Conversely, a given field defined in the reference configuration Ω^f can also be trans-
 99 ported into the current configuration by composition with \mathcal{A}_t^{-1} . For the sake of
 100 simplicity, this composition is omitted. For instance, \mathbf{w} in (2.1)₁ below has to be read
 101 as $\mathbf{w} \circ \mathcal{A}_t^{-1}$.

102 **Coupled problem in strong form.** The considered fluid-structure interaction
 103 model reads as follows: find the fluid domain displacement $\mathbf{d}^f : \Omega^f \times \mathbb{R}^+ \rightarrow \mathbb{R}^d$, the
 104 fluid velocity $\hat{\mathbf{u}} : \Omega^f \times \mathbb{R}^+ \rightarrow \mathbb{R}^d$, the fluid pressure $\hat{p} : \Omega^f \times \mathbb{R}^+ \rightarrow \mathbb{R}$, the solid
 105 displacement $\mathbf{d} : \Omega^s \times \mathbb{R}^+ \rightarrow \mathbb{R}^d$, and the structure velocity $\dot{\mathbf{d}} : \Omega^s \times \mathbb{R}^+ \rightarrow \mathbb{R}^d$ such
 106 that, for all $t > 0$,

$$107 \quad (2.1) \quad \begin{cases} \rho^f \partial_t \mathbf{u} |_{\mathcal{A}} + \rho^f (\mathbf{u} - \mathbf{w}) \cdot \nabla \mathbf{u} - \text{div } \boldsymbol{\sigma}(\mathbf{u}, p) = \mathbf{0} & \text{in } \Omega^f(t), \\ \text{div } \mathbf{u} = 0 & \text{in } \Omega^f(t), \\ \mathbf{u} = \mathbf{0} & \text{on } \Gamma^f, \end{cases}$$

$$108 \quad (2.2) \quad \begin{cases} \rho^s \partial_t \dot{\mathbf{d}} - \text{div}(\mathbf{F}^s \boldsymbol{\Sigma}(\mathbf{d})) = \mathbf{0} & \text{in } \Omega^s, \\ \dot{\mathbf{d}} = \partial_t \mathbf{d} & \text{in } \Omega^s, \\ \mathbf{d} = \mathbf{0} & \text{on } \Gamma^s, \end{cases}$$

$$109 \quad (2.3) \quad \begin{cases} \mathbf{d}^f = \mathcal{L}(\mathbf{d}|_{\Sigma}), \quad \mathbf{w} = \partial_t \mathbf{d}^f, \quad \mathcal{A} = \mathbf{I}_{\Omega^f} + \mathbf{d}^f, \quad \Omega^f(t) = \mathcal{A}(\Omega^f, t), \\ \hat{\mathbf{u}} = \dot{\mathbf{d}} & \text{on } \Sigma, \\ \mathbf{F}^s \boldsymbol{\Sigma}(\mathbf{d}) \mathbf{n}^s = -J \hat{\boldsymbol{\sigma}}(\mathbf{u}, p) \mathbf{F}^{-T} \hat{\mathbf{n}} & \text{on } \Sigma. \end{cases}$$

The constants $\rho^f, \rho^s > 0$ stand, respectively, for the fluid and solid densities, $\partial_t |_{\mathcal{A}} \stackrel{\text{def}}{=}$
 $\partial_t + \mathbf{w} \cdot \nabla$ for the ALE time derivative and $\boldsymbol{\sigma}(\mathbf{u}, p) \stackrel{\text{def}}{=}} 2\mu\boldsymbol{\epsilon}(\mathbf{u}) - p\mathbf{I}$ for the fluid

Cauchy stress tensor, with $\mu > 0$ the fluid dynamic viscosity (supposed constant) and $\boldsymbol{\epsilon}(\mathbf{u}) = \frac{1}{2}(\nabla \mathbf{u} + (\nabla \mathbf{u})^\top)$ the strain rate tensor. The symbol $\mathbf{F}^s \stackrel{\text{def}}{=} \mathbf{I} + \nabla \mathbf{d}$ corresponds to the gradient of deformation of the solid and $\boldsymbol{\Sigma}(\mathbf{d})$ denotes its second Piola-Kirchoff stress tensor which, for an hyper-elastic material, is given in terms of the internal energy functional $W : \mathbb{R}_{\text{sym}}^{d \times d} \rightarrow \mathbb{R}^+$ as

$$\boldsymbol{\Sigma} = \frac{\partial W}{\partial \mathbf{E}}(\mathbf{E}),$$

110 where the symbol \mathbf{E} denotes the Green-Lagrange strain tensor given by the relation
111 $\mathbf{E} \stackrel{\text{def}}{=} \frac{1}{2}((\mathbf{F}^s)^\top \mathbf{F}^s - \mathbf{I})$.

112 Finally, the coupled system (2.1)-(2.3) is complemented with the following initial
113 conditions $\hat{\mathbf{u}}(0) = \hat{\mathbf{u}}_0$ and $\mathbf{d}(0) = \mathbf{d}_0, \dot{\mathbf{d}}(0) = \dot{\mathbf{d}}_0$ in Ω^f and Ω^s , respectively.

114 The relation (2.3)₁ enforces the geometrical compatibility between the fluid and
115 solid domains. Here, the symbol \mathcal{L} represents a smooth lifting operator (possibly
116 non-linear) from Σ over Ω^f , which vanishes on Γ^f . The remaining interface conditions
117 (2.3)_{2,3} enforce, respectively, the so-called interface kinematic and dynamic coupling.

Weak form and energy identity. We consider the following functional spaces:

$$\mathbf{V}^f \subset \{\mathbf{v} \in \mathbf{H}^1(\Omega^f) : \mathbf{v}|_{\Gamma^f} = \mathbf{0}\}, \quad M^f \stackrel{\text{def}}{=} L^2(\Omega^f), \quad \mathbf{V}^s \subset \{\mathbf{v} \in \mathbf{H}^1(\Omega^s) : \mathbf{v}|_{\Gamma^s} = \mathbf{0}\}.$$

118 Let $(\hat{\mathbf{u}}, \hat{p}, \mathbf{d}, \dot{\mathbf{d}})$ be solution of the coupled system (2.1)–(2.3), one can show that the
119 following monolithic variational formulation holds (see, e.g., [16]), for $t > 0$,

$$(2.4) \quad \begin{aligned} 120 \quad & \rho^f \frac{d}{dt} \int_{\Omega^f(t)} \mathbf{u} \cdot \mathbf{v} - \rho^f \int_{\Omega^f(t)} (\operatorname{div} \mathbf{w}) \mathbf{u} \cdot \mathbf{v} + \rho^f \int_{\Omega^f(t)} (\mathbf{u} - \mathbf{w}) \cdot \nabla \mathbf{u} \cdot \mathbf{v} + 2\mu \int_{\Omega^f(t)} \boldsymbol{\epsilon}(\mathbf{u}) : \boldsymbol{\epsilon}(\mathbf{v}) \\ 121 \quad & - \int_{\Omega^f(t)} p \operatorname{div} \mathbf{v} + \int_{\Omega^f(t)} q \operatorname{div} \mathbf{u} + \rho^s \int_{\Omega^s} \partial_t \dot{\mathbf{d}} \cdot \boldsymbol{\xi} + \int_{\Omega^s} \boldsymbol{\Sigma} : \partial_{\mathbf{d}}(\mathbf{E}) \boldsymbol{\xi} = 0 \end{aligned}$$

122 for all $(\hat{\mathbf{v}}, \hat{q}, \boldsymbol{\xi}) \in \mathbf{V}^f \times M^f \times \mathbf{V}^s$ with $\hat{\mathbf{v}}|_{\Sigma} = \boldsymbol{\xi}|_{\Sigma}$, and where we have used the notation

$$123 \quad (2.5) \quad \partial_{\mathbf{d}}(\mathbf{E}) \boldsymbol{\xi} \stackrel{\text{def}}{=} \frac{1}{2} \left[(\mathbf{F}^s)^\top \nabla \boldsymbol{\xi} + (\nabla \boldsymbol{\xi})^\top \mathbf{F}^s \right],$$

124 for the differential of \mathbf{E} applied to $\boldsymbol{\xi}$.

125 By testing (2.4) with $(\hat{\mathbf{v}}, \hat{q}, \boldsymbol{\xi}) = (\hat{\mathbf{u}}, \hat{p}, \dot{\mathbf{d}})$ and using standard arguments, we can
126 obtain the following classical energy identity (see, e.g., [16]):

$$(2.6) \quad \begin{aligned} 127 \quad & \frac{\rho^f}{2} \|\mathbf{u}\|_{0, \Omega^f(t)}^2 + \frac{\rho^s}{2} \|\dot{\mathbf{d}}\|_{0, \Omega^s}^2 + \int_{\Omega^s} W(\mathbf{E}(\mathbf{d})) + 2\mu \int_0^t \|\boldsymbol{\epsilon}(\mathbf{u}(s))\|_{0, \Omega^f(s)}^2 ds \\ 128 \quad & = \frac{\rho^f}{2} \|\mathbf{u}_0\|_{0, \Omega^f(0)}^2 + \frac{\rho^s}{2} \|\dot{\mathbf{d}}_0\|_{0, \Omega^s}^2 + \frac{1}{2} \int_{\Omega^s} W(\mathbf{E}(\mathbf{d}_0)). \end{aligned}$$

129 Here, the first two terms represent the kinetic energy of the fluid and solid, respec-
130 tively. The third term takes into account the hyperelastic energy of the solid, and the
131 fourth term corresponds to the viscous dissipation of the fluid.

132 **3. Robin-Robin explicit coupling scheme.** The purpose of this section is to
133 formulate the Robin-Robin loosely coupled scheme of [6, 8] in the framework of the
134 non-linear coupled problem (2.1)-(2.3).

Time semi-discretization. In what follows, the scalar $\tau > 0$ denotes the time-step length and $\{t_n \stackrel{\text{def}}{=} n\tau\}_{n \in \mathbb{N}}$ represents the temporal grid. We shall also make use of the following notations:

$$\partial_\tau x^n \stackrel{\text{def}}{=} \frac{1}{\tau}(x^n - x^{n-1}), \quad x^{n-\frac{1}{2}} \stackrel{\text{def}}{=} \frac{1}{2}(x^n + x^{n-1}),$$

135 for the first-order backward difference and the mid-point value, respectively. More-
136 over, for a given time-dependent quantity $x(t)$, we will use the notation $x^n \stackrel{\text{def}}{=} x(t_n)$.

137 The bulk terms of the fluid sub-system (2.1) will be discretized in time with
138 a backward-Euler semi-implicit scheme, whereas for the solid sub-system (2.2) we
139 consider a mid-point scheme with the so-called Gonzalez correction (see [23]). Finally,
140 for the time discretization of the interface conditions (2.3), we combine an explicit
141 treatment of the geometrical compatibility with a Robin-Robin type splitting of the
142 kinematic and dynamic interface conditions, originally proposed in [8] for the linear
143 case. By introducing the following notation for the interfacial fluid stresses on the
144 reference configuration,

$$145 \quad (3.1) \quad \lambda^n \stackrel{\text{def}}{=} J^n \hat{\boldsymbol{\sigma}}(\mathbf{u}^n, p^n) (\mathbf{F}^n)^{-\top} \hat{\mathbf{n}} \quad \text{on } \Sigma,$$

146 the resulting time-stepping procedure can formally be written as follows:

147 • Solve solid:

$$148 \quad (3.2) \quad \left\{ \begin{array}{l} \rho^s \partial_\tau \dot{\mathbf{d}}^n - \mathbf{div} \left(\mathbf{F}^{s, n-\frac{1}{2}} \bar{\boldsymbol{\Sigma}}^{n-\frac{1}{2}} \right) = \mathbf{0} \quad \text{in } \Omega^s, \\ \dot{\mathbf{d}}^{n-\frac{1}{2}} = \partial_\tau \mathbf{d}^n \quad \text{in } \Omega^s, \\ \mathbf{d}^n = \mathbf{0} \quad \text{on } \Gamma^s, \\ \mathbf{F}^{s, n-\frac{1}{2}} \bar{\boldsymbol{\Sigma}}^{n-\frac{1}{2}} \mathbf{n}^s + \alpha (\dot{\mathbf{d}}^{n-\frac{1}{2}} - \hat{\mathbf{u}}^{n-1}) = -\lambda^{n-1} \quad \text{on } \Sigma. \end{array} \right.$$

149 • Fluid domain update:

$$150 \quad (3.3) \quad \mathbf{d}^{f, n} = \mathcal{L}(\mathbf{d}^n|_\Sigma), \quad \mathbf{w}^n = \partial_\tau \mathbf{d}^{f, n}, \quad \mathcal{A}^n = \mathbf{I}_{\Omega^f} + \mathbf{d}^{f, n}, \quad \Omega^{f, n} = \mathcal{A}^n(\Omega^f).$$

151 • Solve fluid:

$$152 \quad (3.4) \quad \left\{ \begin{array}{l} \rho^f \partial_\tau \mathbf{u}^n|_{\mathcal{A}} + \rho^f (\mathbf{u}^{n-1} - \mathbf{w}^n) \cdot \nabla \mathbf{u}^n - \mathbf{div} \boldsymbol{\sigma}(\mathbf{u}^n, p^n) = \mathbf{0} \quad \text{in } \Omega^{f, n}, \\ \mathbf{div} \mathbf{u}^n = 0 \quad \text{in } \Omega^{f, n}, \\ \mathbf{u}^n = \mathbf{0} \quad \text{on } \Gamma^f, \\ \lambda^n + \alpha (\hat{\mathbf{u}}^n - \dot{\mathbf{d}}^{n-\frac{1}{2}}) = \lambda^{n-1} \quad \text{on } \Sigma. \end{array} \right.$$

153 Here, the symbol $\bar{\boldsymbol{\Sigma}}^{n-\frac{1}{2}}$ denotes the mid-point correction of the solid stress given by
154 (see [23]):

$$155 \quad (3.5) \quad \bar{\boldsymbol{\Sigma}}^{n-\frac{1}{2}} \stackrel{\text{def}}{=} \boldsymbol{\Sigma}^{n-\frac{1}{2}} + \frac{\partial_\tau W(\mathbf{E}^n) - \frac{\partial W}{\partial \mathbf{E}}(\mathbf{E}^{n-\frac{1}{2}}) : \partial_\tau \mathbf{E}^n}{|\partial_\tau \mathbf{E}^n|^2} \partial_\tau \mathbf{E}^n,$$

156 which guarantees energy stability in the solid, and the scalar $\alpha > 0$ stands for the user-
157 defined Robin parameter of the fluid-solid splitting. Note that the above interfacial

158 Robin-Robin splitting, viz.,

$$159 \quad (3.6) \quad \begin{cases} \mathbf{F}^{\text{s},n-\frac{1}{2}} \bar{\Sigma}^{n-\frac{1}{2}} \mathbf{n}^{\text{s}} + \alpha (\dot{\mathbf{d}}^{n-\frac{1}{2}} - \hat{\mathbf{u}}^{n-1}) = -\boldsymbol{\lambda}^{n-1} & \text{on } \Sigma, \\ \boldsymbol{\lambda}^n + \alpha (\hat{\mathbf{u}}^n - \dot{\mathbf{d}}^{n-\frac{1}{2}}) = \boldsymbol{\lambda}^{n-1} & \text{on } \Sigma, \end{cases}$$

160 is written in the reference configuration of the interface.

161 **Space discretization, fully discrete scheme.** For the spatial discretization of
 162 (3.2)–(3.4), we adopt a finite element approximation. Let \mathcal{T}_h^{f} and \mathcal{T}_h^{s} be, respectively,
 163 simplicial triangulations of Ω^{f} and Ω^{s} . We assume that \mathcal{T}_h^{f} and \mathcal{T}_h^{s} match on the
 164 interface Σ . We then define the following finite element spaces:

$$165 \quad \mathbf{V}_h^{\text{s}} \stackrel{\text{def}}{=} \{ \mathbf{v} \in \mathbf{V}^{\text{s}} : \mathbf{v}|_K \in \mathbb{P}^1(K), \forall K \in \mathcal{T}_h^{\text{s}} \}, \quad \mathbf{V}_h^{\text{f}} \stackrel{\text{def}}{=} \{ \mathbf{v} \in \mathbf{V}^{\text{f}} : \mathbf{v}|_K \in \mathbb{P}^1(K), \forall K \in \mathcal{T}_h^{\text{f}} \},$$

$$166 \quad M_h^{\text{f}} \stackrel{\text{def}}{=} \{ v \in M^{\text{f}} : v|_K \in \mathbb{P}^1(K), \forall K \in \mathcal{T}_h^{\text{f}} \},$$

167 Since the fluid and solid meshes are assumed to match at the interface, we can define
 168 the discrete traces space

$$169 \quad (3.7) \quad \mathbf{V}_h^{\text{g}} \stackrel{\text{def}}{=} \text{Tr}_{\Sigma} \mathbf{V}_h^{\text{f}} = \text{Tr}_{\Sigma} \mathbf{V}_h^{\text{s}}.$$

170 The fluid bi-linear form is given by

$$171 \quad (3.8) \quad a_{\Omega^{\text{f}},n}(\mathbf{u}_h^{n-1}, \mathbf{w}_h^n; (\mathbf{u}_h^n, p_h^n), (\mathbf{v}_h, q_h)) \stackrel{\text{def}}{=} \rho^{\text{f}} \int_{\Omega^{\text{f}},n} (\mathbf{u}_h^{n-1} - \mathbf{w}_h^n) \cdot \nabla \mathbf{u}_h^n \cdot \mathbf{v}_h$$

$$+ \frac{\rho^{\text{f}}}{2} \int_{\Omega^{\text{f}},n} (\text{div } \mathbf{u}_h^{n-1}) \mathbf{u}_h^n \cdot \mathbf{v}_h$$

$$- \frac{\rho^{\text{f}}}{2} \int_{\Sigma^n} (\mathbf{u}_h^{n-1} - \dot{\mathbf{d}}_h^{n-\frac{1}{2}}) \cdot \mathbf{n} \mathbf{u}_h^n \cdot \mathbf{v}_h$$

$$+ 2\mu \int_{\Omega^{\text{f}},n} \boldsymbol{\epsilon}_h(\mathbf{u}_h^n) : \boldsymbol{\epsilon}_h(\mathbf{v}_h) - \int_{\Omega^{\text{f}},n} p_h^n \text{div } \mathbf{v}_h$$

$$+ \int_{\Omega^{\text{f}},n} q_h \text{div } \mathbf{u}_h^n$$

$$+ s_h^{\text{f}}(\mathbf{u}_h^{n-1}, \mathbf{w}_h^n; (\mathbf{u}_h^n, p_h^n), (\mathbf{v}_h, q_h)).$$

The second term in (3.8) corresponds to the so-called Temam's trick, which copes with the fact that the discrete fluid velocities are not divergence free. The third term is a weakly consistent stabilization term which allows to control the energy contributions of the convective term (first term of (3.8)) induced by the fact that

$$\hat{\mathbf{u}}_h^{n-1}|_{\Sigma} \neq \mathbf{w}_h^n|_{\Sigma} = \dot{\mathbf{d}}_h^{n-\frac{1}{2}}|_{\Sigma}.$$

172 Following [28, Chapter 5], we introduce a second weakly consistent stabilization term,
 173 namely,

$$174 \quad (3.9) \quad s_{\Omega^{\text{f}},n}(\mathbf{u}_h^n, \mathbf{v}_h) \stackrel{\text{def}}{=} -\frac{\rho^{\text{f}}}{2\tau} \left(\int_{\Omega^{\text{f}},n} \mathbf{u}_h^n \cdot \mathbf{v}_h - \int_{\Omega^{\text{f}},n-1} \mathbf{u}_h^n \cdot \mathbf{v}_h \right) + \frac{\rho^{\text{f}}}{2} \int_{\Omega^{\text{f}},n} (\text{div } \mathbf{w}_h^n) \mathbf{u}_h^n \cdot \mathbf{v}_h,$$

whose purpose is to cope with the issues related to the so-called discrete geometric conservation law (see, e.g., [14]). Note that the weak consistency of (3.9) is a

consequence of the Reynolds transport formula:

$$\frac{d}{dt} \int_{\Omega^f(t)} q = \int_{\Omega^f(t)} q \operatorname{div} \mathbf{w}$$

for any smooth enough field $\hat{q}: \Omega^f \rightarrow \mathbb{R}^+$. Finally, the non-negative bi-linear term,

$$s_h^f(\mathbf{u}_h^{n-1}, \mathbf{w}_h^n; (\mathbf{u}_h^n, p_h^n), (\mathbf{v}_h, q_h)),$$

175 stands for any given velocity and pressure stabilization operator (see, e.g., [29, 11]),
 176 whose purpose is to circumvent the issues related to the lack of robustness for both
 177 high local Reynolds numbers and the lack of inf-sup stability for the pair \mathbf{V}_h^f/M^f .

Algorithm 3.1 Explicit Robin-Robin scheme (fully discrete)

Assume \mathbf{u}_h^0 , \mathbf{d}_h^0 and $\mathbf{d}_h^{f,0}$, $\boldsymbol{\lambda}_h^0$ to be given and, for $n \geq 1$, perform:

- Solve solid: find $(\mathbf{d}_h^n, \dot{\mathbf{d}}_h^n) \in \mathbf{V}_h^s \times \mathbf{V}_h^s$, with $\dot{\mathbf{d}}_h^{n-\frac{1}{2}} = \partial_\tau \mathbf{d}_h^n$ such that

$$(3.10) \quad \rho^s \int_{\Omega^s} \partial_\tau \dot{\mathbf{d}}_h^n \cdot \boldsymbol{\xi}_h + \int_{\Omega^s} \bar{\boldsymbol{\Sigma}}_h^{n-\frac{1}{2}} : \partial_d (\mathbf{E}_h^{n-\frac{1}{2}}) \boldsymbol{\xi}_h + \alpha \int_\Sigma (\dot{\mathbf{d}}_h^{n-\frac{1}{2}} - \hat{\mathbf{u}}_h^{n-1}) \cdot \boldsymbol{\xi}_h \\ = - \int_\Sigma \boldsymbol{\lambda}_h^{n-1} \cdot \boldsymbol{\xi}_h$$

for all $\boldsymbol{\xi}_h \in \mathbf{V}_h^s$.

- Update fluid domain:

$$\mathbf{d}_h^{f,n} = \mathcal{L}_h(\mathbf{d}_h^n|_\Sigma), \quad \mathbf{w}_h^n = \partial_\tau \mathbf{d}_h^{f,n}, \quad \mathcal{A}_h^n = \mathbf{I}_{\Omega^f} + \mathbf{d}_h^{f,n}, \quad \Omega^{f,n} = \mathcal{A}_h^n(\Omega^f).$$

- Solve fluid: find $(\hat{\mathbf{u}}_h^n, \hat{p}^n) \in \mathbf{V}_h^f \times Q_h$ such that

$$(3.11) \quad \frac{\rho^f}{\tau} \left(\int_{\Omega^{f,n}} \mathbf{u}_h^n \cdot \mathbf{v}_h - \int_{\Omega^{f,n-1}} \mathbf{u}_h^{n-1} \cdot \mathbf{v}_h \right) - \rho^f \int_{\Omega^{f,n}} (\operatorname{div} \mathbf{w}_h^n) \mathbf{u}_h^n \cdot \mathbf{v}_h \\ + s_{\Omega^{f,n}}(\mathbf{u}_h^n, \mathbf{v}_h) + a_{\Omega^{f,n}}(\mathbf{u}_h^{n-1}, \mathbf{w}_h^n; (\mathbf{u}_h^n, p_h^n), (\mathbf{v}_h, q_h)) \\ + \alpha \int_\Sigma (\hat{\mathbf{u}}_h^n - \dot{\mathbf{d}}_h^{n-\frac{1}{2}}) \cdot \hat{\mathbf{v}}_h = \int_\Sigma \boldsymbol{\lambda}_h^{n-1} \cdot \hat{\mathbf{v}}_h$$

for all $(\hat{\mathbf{v}}_h, \hat{q}_h) \in \mathbf{V}_h^f \times Q_h$.

- Fluid-stress update: set $\boldsymbol{\lambda}_h^n \in \mathbf{V}_h^g$ as

$$(3.12) \quad \boldsymbol{\lambda}_h^n = \boldsymbol{\lambda}_h^{n-1} + \alpha (\dot{\mathbf{d}}_h^{n-\frac{1}{2}} - \hat{\mathbf{u}}_h^n) \quad \text{on } \Sigma.$$

178 With all the above ingredients, the proposed fully discrete counterpart of (3.2)–
 179 (3.4) is detailed in Algorithm 3.1.

180 Some remarks are now in order. The relation (3.12) in Algorithm 3.1 is essentially
 181 a rewriting of (3.6)₂, in which the intermediate variable $\boldsymbol{\lambda}_h^n$ represents the discrete
 182 counterpart of the interfacial fluid stress on the reference configuration $\boldsymbol{\lambda}^n$, given by
 183 (3.1). Indeed, by combining (3.11) and (3.12), the update of the fluid-stress in the
 184 fourth step of Algorithm 3.1 can be formulated, in a more standard form as a fluid

185 variational residual (see, e.g., [15]):

$$\begin{aligned}
186 \quad (3.13) \quad & \int_{\Sigma} \boldsymbol{\lambda}_h^n \cdot \boldsymbol{\mu}_h = \frac{\rho^f}{\tau} \left(\int_{\Omega^{f,n}} \mathbf{u}_h^n \cdot \mathcal{L}_h^f \boldsymbol{\mu}_h - \int_{\Omega^{f,n-1}} \mathbf{u}_h^{n-1} \cdot \mathcal{L}_h^f \boldsymbol{\mu}_h \right) \\
187 \quad & - \rho^f \int_{\Omega^{f,n}} (\operatorname{div} \mathbf{w}_h^n) \mathbf{u}_h^n \cdot \mathcal{L}_h^f \boldsymbol{\mu}_h + a_{\Omega^{f,n}}(\mathbf{u}_h^{n-1}, \mathbf{w}_h^n; (\mathbf{u}_h^n, p_h^n), (\mathcal{L}_h^f \boldsymbol{\mu}_h, 0))
\end{aligned}$$

for all $\boldsymbol{\mu}_h \in \mathbf{V}_h^g$ and where $\mathcal{L}_h^f : \mathbf{V}_h^g \rightarrow \mathbf{V}_h^f$ represents a linear fluid-sided lifting operator, such that, the nodal values of $\mathcal{L}_h^f \boldsymbol{\mu}_h$ vanish out of Σ and $(\mathcal{L}_h^f \boldsymbol{\mu}_h)|_{\Sigma} = \boldsymbol{\mu}_h$, for all $\boldsymbol{\mu}_h \in \mathbf{V}_h^g$. We can hence see that, as indicated above, $\boldsymbol{\lambda}_h^n$ is nothing but the discrete counterpart of the interfacial fluid stress on the reference configuration. It is worth noting that the interfacial stabilization term in (3.8) introduces a weakly consistent perturbation of the fluid stresses approximation provided by (3.13). Indeed, this relation formally writes

$$\int_{\Sigma} \boldsymbol{\lambda}_h^n \cdot \boldsymbol{\mu}_h \equiv \int_{\Sigma^n} \boldsymbol{\sigma}(\mathbf{u}_h^n, p_h^n) \mathbf{n}_h \cdot \boldsymbol{\mu}_h - \frac{\rho^f}{2} \int_{\Sigma^n} (\mathbf{u}_h^{n-1} - \dot{\mathbf{d}}_h^{n-\frac{1}{2}} \circ (\mathcal{A}_h^n)^{-1}) \cdot \mathbf{n}_h (\mathbf{u}_h^n \cdot \boldsymbol{\mu}_h)$$

for all $\boldsymbol{\mu} \in \mathbf{V}_h^g$, or point-wise

$$\boldsymbol{\lambda}^n \equiv J^n \widehat{\boldsymbol{\sigma}}(\mathbf{u}^n, p^n) (\mathbf{F}^n)^{-T} \widehat{\mathbf{n}} - \frac{\rho^f J^n}{2} (\widehat{\mathbf{u}}^{n-1} - \dot{\mathbf{d}}^{n-\frac{1}{2}}) \cdot ((\mathbf{F}^n)^{-T} \widehat{\mathbf{n}}) \widehat{\mathbf{u}}^n \quad \text{on } \Sigma.$$

188 It should also be noted that these last two expressions are merely formal and, there-
189 fore, can not be used in the energy stability analysis of Algorithm 3.1, presented in
190 Section 3.1 below.

191 Algorithm 3.1 shares some similarities with the time-semidiscrete Robin-Robin
192 scheme proposed in [27], but with several fundamental differences. First, the method
193 is here formulated in a fully discrete setting, with a rigorous definition of the interfacial
194 fluid-stresses. Second, a suitable interfacial stabilization is added to control the energy
195 contributions of the convective term. This avoids the artificial modifications of the
196 fluid velocity on the interface advocated in [27, Section 3]. Third, the stability of the
197 method reported in the next paragraph also holds in 3D, irrespectively of the discrete
198 geometric conservation law, via the stabilization term (3.9). Finally, the stability
199 analysis (Section 3.1) and the numerical examples (of Section 5) cover the case of the
200 coupling with a general non-linear solid model.

201 **3.1. Energy stability analysis.** For $n \geq 1$, let the discrete energy and dissi-
202 pation be respectively defined as

$$\begin{aligned}
E_h^n & \stackrel{\text{def}}{=} \frac{\rho^f}{2} \|\mathbf{u}_h^n\|_{0,\Omega^{f,n}}^2 + \frac{\rho^s}{2} \|\dot{\mathbf{d}}_h^n\|_{0,\Omega^s}^2 + \int_{\Omega^s} W(\mathbf{E}_h^n) + \frac{\tau}{2} \left(\alpha \|\widehat{\mathbf{u}}_h^n\|_{0,\Sigma}^2 + \frac{1}{\alpha} \|\boldsymbol{\lambda}_h^n\|_{0,\Sigma}^2 \right), \\
G_h^n & \stackrel{\text{def}}{=} \sum_{m=1}^n \tau \left(2\mu \|\boldsymbol{\epsilon}(\mathbf{u}_h^m)\|_{0,\Omega^{f,m}}^2 + \alpha \|\dot{\mathbf{d}}_h^{m-\frac{1}{2}} - \widehat{\mathbf{u}}_h^{m-1}\|_{0,\Sigma}^2 \right).
\end{aligned}$$

203 **THEOREM 1.** *Let $\{(\widehat{\mathbf{u}}^n, \widehat{p}^n, \mathbf{d}^n, \dot{\mathbf{d}}^n, \boldsymbol{\lambda}^n)\}_{n \geq 1}$ be given by Algorithm 3.1. The follow-*
204 *ing energy estimate holds for $n \geq 1$*

$$205 \quad (3.14) \quad E_h^n + G_h^n \leq E_h^0.$$

206 *As a result, Algorithm 3.1 is unconditionally stable in the energy norm.*

229 Next, we proceed to add the energy contributions of the solid, as given by (3.17),
 230 and the fluid, as expressed in (3.19). This results in the following energy expression:

$$231 \quad (3.20) \quad \frac{\rho^f}{2} \partial_\tau \|\mathbf{u}_h^n\|_{0,\Omega^f,n}^2 + \frac{\rho^s}{2} \partial_\tau \|\dot{\mathbf{d}}_h^n\|_{0,\Omega^s}^2 + \partial_\tau \int_{\Omega^s} W(\mathbf{E}_h^n) + 2\mu \|\boldsymbol{\epsilon}(\mathbf{u}_h^n)\|_{0,\Omega^f,n}^2 \leq R_h^n,$$

where

$$R_h^n \stackrel{\text{def}}{=} \alpha \int_{\Sigma} (\widehat{\mathbf{u}}_h^{n-1} - \dot{\mathbf{d}}_h^{n-\frac{1}{2}}) \cdot \dot{\mathbf{d}}_h^{n-\frac{1}{2}} - \int_{\Sigma} \boldsymbol{\lambda}_h^{n-1} \cdot \dot{\mathbf{d}}_h^{n-\frac{1}{2}} + \int_{\Sigma} \boldsymbol{\lambda}_h^n \cdot \widehat{\mathbf{u}}_h^n.$$

232 We can now proceed as in the case with a fixed domain [6], which yields

$$233 \quad (3.21) \quad R_h^n = \frac{\alpha}{2} (\|\widehat{\mathbf{u}}_h^{n-1}\|_{0,\Sigma}^2 - \|\widehat{\mathbf{u}}_h^n\|_{0,\Sigma}^2) + \frac{1}{2\alpha} (\|\boldsymbol{\lambda}_h^{n-1}\|_{0,\Sigma}^2 - \|\boldsymbol{\lambda}_h^n\|_{0,\Sigma}^2) - \alpha \|\dot{\mathbf{d}}_h^{n-\frac{1}{2}} - \widehat{\mathbf{u}}_h^{n-1}\|_{0,\Sigma}^2,$$

234 Finally, by inserting (3.21) into (3.20), we obtain

$$235 \quad \frac{\rho^f}{2} \partial_\tau \|\mathbf{u}_h^n\|_{0,\Omega^f,n}^2 + \frac{\rho^s}{2} \partial_\tau \|\dot{\mathbf{d}}_h^n\|_{0,\Omega^s}^2 + \partial_\tau \int_{\Omega^s} W(\mathbf{E}_h^n) + 2\mu \|\boldsymbol{\epsilon}(\mathbf{u}_h^n)\|_{0,\Omega^f,n}^2 \\ 236 \quad + \frac{\alpha}{2} \|\widehat{\mathbf{u}}_h^n\|_{0,\Sigma}^2 + \frac{\tau}{2\alpha} \|\boldsymbol{\lambda}_h^n\|_{0,\Sigma}^2 + \alpha \|\dot{\mathbf{d}}_h^{n-\frac{1}{2}} - \widehat{\mathbf{u}}_h^{n-1}\|_{0,\Sigma}^2 \leq \frac{\alpha}{2} \|\widehat{\mathbf{u}}_h^{n-1}\|_{0,\Sigma}^2 + \frac{1}{2\alpha} \|\boldsymbol{\lambda}_h^{n-1}\|_{0,\Sigma}^2.$$

237 The energy estimate (3.14) then follows by multiplying the previous expression by τ
 238 and then summing over $m = 1, \dots, n$, which completes the proof. \square

239 **4. Error estimate in a linearized setting.** In this section, we provide an
 240 error analysis of Algorithm 3.1 in a simplified setting. To this purpose, we assume
 241 that the solid undergoes infinitesimal displacements and that convective effects are
 242 negligible in the fluid. Under these assumptions, the non-linear coupled problem (2.1)-
 243 (2.3) can be replaced by the following linear Stokes-elasticity system in the reference
 244 configuration $\Omega^f \cup \Omega^s$:

$$245 \quad (4.1) \quad \begin{cases} \rho^f \partial_t \mathbf{u} - \operatorname{div} \boldsymbol{\sigma}(\mathbf{u}, p) = \mathbf{0} & \text{in } \Omega^f \times (0, T), \\ \operatorname{div} \mathbf{u} = 0 & \text{in } \Omega^f \times (0, T), \\ \mathbf{u} = \mathbf{0} & \text{on } \Gamma^f \times (0, T), \end{cases}$$

$$246 \quad (4.2) \quad \begin{cases} \rho^s \partial_t \dot{\mathbf{d}} - \operatorname{div} \boldsymbol{\sigma}(\dot{\mathbf{d}}) = \mathbf{0} & \text{in } \Omega^s \times (0, T), \\ \dot{\mathbf{d}} = \partial_t \mathbf{d} & \text{in } \Omega^s \times (0, T), \\ \dot{\mathbf{d}} = \mathbf{0} & \text{on } \Gamma^s \times (0, T), \end{cases}$$

$$247 \quad (4.3) \quad \begin{cases} \mathbf{u} = \dot{\mathbf{d}} & \text{on } \Sigma \times (0, T), \\ \boldsymbol{\sigma}(\mathbf{u}, p) \mathbf{n} = \boldsymbol{\sigma}(\dot{\mathbf{d}}) \mathbf{n} & \text{on } \Sigma \times (0, T), \end{cases}$$

complemented with the initial conditions: $\mathbf{d}(0, \cdot) = \mathbf{d}_0$, $\dot{\mathbf{d}}(0, \cdot) = \dot{\mathbf{d}}_0$ in Ω^s , and $\mathbf{u}(0, \cdot) = \mathbf{u}_0$ in Ω^f and where $T > 0$ denotes the final time. The symbol $\boldsymbol{\sigma}(\dot{\mathbf{d}})$ stands for the linearized solid stress tensor, which is assumed to be given in terms of the solid displacement $\dot{\mathbf{d}}$ by the following relation:

$$\boldsymbol{\sigma}(\dot{\mathbf{d}}) \stackrel{\text{def}}{=} 2L_1 \boldsymbol{\epsilon}(\dot{\mathbf{d}}) + L_2 (\operatorname{div} \dot{\mathbf{d}}) \mathbf{I},$$

248 where $L_1, L_2 > 0$ denote the so called Lamé coefficients of the solid.

249 Assuming that $\boldsymbol{\lambda} \in L^2(\Sigma)$, the solution of (4.1)–(4.3) satisfies the weak formula-
250 tion

$$\begin{aligned}
 & \rho^s \int_{\Omega^s} \partial_t \dot{\mathbf{d}} \cdot \boldsymbol{\xi} + a^s(\mathbf{d}, \boldsymbol{\xi}) + \int_{\Sigma} \boldsymbol{\lambda} \cdot \boldsymbol{\xi} = 0, \\
 & \int_{\Omega^s} \dot{\mathbf{d}} \cdot \boldsymbol{\phi} - \int_{\Omega^s} \partial_t \mathbf{d} \cdot \boldsymbol{\phi} = 0, \\
 251 \quad (4.4) \quad & \rho^f \int_{\Omega^f} \partial_\tau \mathbf{u} \cdot \mathbf{v} + a^f((\mathbf{u}, p), (\mathbf{v}, q)) - \int_{\Sigma} \boldsymbol{\lambda} \cdot \mathbf{v} = 0, \\
 & \int_{\Sigma} (\mathbf{u} - \dot{\mathbf{d}}) \cdot \boldsymbol{\mu} = 0
 \end{aligned}$$

252 for all $(\boldsymbol{\xi}, \boldsymbol{\phi}, \mathbf{v}, q) \in \mathbf{V}^s \times \mathbf{V}^s \times \mathbf{V}^f \times M^f$. Here, the bilinear forms of the fluid, denoted
253 as a^f , and of the solid, denoted as a^s , are respectively given by

$$\begin{aligned}
 254 \quad a^f((\mathbf{u}, p), (\mathbf{v}, q)) & \stackrel{\text{def}}{=} 2\mu \int_{\Omega^f} \boldsymbol{\epsilon}(\mathbf{u}) : \boldsymbol{\epsilon}(\mathbf{v}) - \int_{\Omega^f} p \operatorname{div} \mathbf{v} + \int_{\Omega^f} q \operatorname{div} \mathbf{u}, \\
 255 \quad a^s(\mathbf{d}, \boldsymbol{\xi}) & \stackrel{\text{def}}{=} 2L_1 \int_{\Omega^s} \boldsymbol{\epsilon}(\mathbf{d}) : \boldsymbol{\epsilon}(\boldsymbol{\xi}) + L_2 \int_{\Omega^s} (\operatorname{div} \mathbf{d})(\operatorname{div} \boldsymbol{\xi}).
 \end{aligned}$$

We also introduce the elastic energy norm of the solid given by the relation

$$\|\boldsymbol{\xi}\|_s \stackrel{\text{def}}{=} \sqrt{a^s(\boldsymbol{\xi}, \boldsymbol{\xi})}$$

256 for all $\boldsymbol{\xi} \in \mathbf{V}^s$.

257 For the numerical approximation of (4.4) we consider the Robin-Robin loosely
258 coupled scheme introduced in [6] and detailed in Algorithm 4.1. As in Section 3, we
259 employ a backward Euler method for the fluid and a mid-point scheme for the solid.
260 In addition, for the spatial discretization, we consider a piecewise affine continuous
261 finite elements, where we assume that the fluid and solid meshes are fitted. In other
262 words, Algorithm 4.1 is essentially the linear counterpart of Algorithm 3.1. Here, we
263 accommodate for the lack of inf-sup stability by using a pressure stabilized bilinear
264 form for the fluid (see [4]),

$$265 \quad (4.5) \quad a_h^f((\mathbf{u}_h, p_h), (\mathbf{v}_h, q_h)) \stackrel{\text{def}}{=} a^f((\mathbf{u}_h, p_h), (\mathbf{v}_h, q_h)) + \frac{\gamma_p h^2}{\mu} \int_{\Omega^f} \nabla p_h \cdot \nabla q_h,$$

266 with $\gamma_p > 0$ a user-defined parameter.

267 **4.1. Relation to previous results.** In [6], we proved that Algorithm 4.1 was
268 optimal in space and sub-optimal in time, specifically $\mathcal{O}(h + \tau^{\frac{1}{2}})$. However, following
269 new numerical experiments and the results of [7], it has become clear that the result
270 in [6] is not a strict bound. Following the techniques developed in [7], we are able
271 to prove that the Robin-Robin scheme for the linear case is, in fact, nearly-optimal
272 in time. This result is presented below, along with the main features of the analysis.
273 The full analysis is covered in detail in [13, Chapter 5].

274 **4.2. Nearly-optimal error estimate.** In what follows, $N \in \mathbb{N}$ is such that
275 $N\tau \leq T$ and let $\{(\mathbf{u}_h^n, p_h^n, \boldsymbol{\lambda}_h^n, \mathbf{d}_h^n, \dot{\mathbf{d}}_h^n)\}_{1 \leq n \leq N} \subset \mathbf{V}_h^f \times M_h^f \times \mathbf{V}_h^g \times \mathbf{V}_h^s \times \mathbf{V}_h^s$ be given
276 by Algorithm 4.1. We introduce the discrete error terms

$$277 \quad \mathbf{e}_{\mathbf{d},h}^n \stackrel{\text{def}}{=} \mathbf{d}_h^n - R_h^s \mathbf{d}^n, \quad \mathbf{e}_{\dot{\mathbf{d}},h}^n \stackrel{\text{def}}{=} \dot{\mathbf{d}}_h^n - R_h^s \dot{\mathbf{d}}^n,$$

Algorithm 4.1 Robin-based loosely coupled scheme (linear case).

Assume \mathbf{u}_h^0 , \mathbf{d}_h^0 and $\mathbf{d}_h^{f,0}$, $\boldsymbol{\lambda}_h^0$ to be given and, for $n \geq 1$, perform:

1. Solid subproblem: Find $\dot{\mathbf{d}}_h^n, \mathbf{d}_h^n \in \mathbf{V}_h^s$ such that $\dot{\mathbf{d}}_h^{n-\frac{1}{2}} = \partial_\tau \mathbf{d}_h^n$ and

$$(4.6) \quad \rho^s \int_{\Omega^s} \partial_\tau \dot{\mathbf{d}}_h^n \cdot \boldsymbol{\xi}_h + a^s(\mathbf{d}_h^{n-\frac{1}{2}}, \boldsymbol{\xi}_h) + \alpha \int_\Sigma (\dot{\mathbf{d}}_h^{n-\frac{1}{2}} - \mathbf{u}_h^{n-1}) \cdot \boldsymbol{\xi}_h = - \int_\Sigma \boldsymbol{\lambda}_h^{n-1} \cdot \boldsymbol{\xi}_h$$

for all $\boldsymbol{\xi}_h \in \mathbf{V}_h^s$.

2. Fluid subproblem: Find $(\mathbf{u}_h^n, p_h^n) \in \mathbf{V}_h^f \times M_h^f$ such that

$$(4.7) \quad \rho^f \int_{\Omega^f} \partial_\tau \mathbf{u}_h^n \cdot \mathbf{v}_h + a_h^f((\mathbf{u}_h^n, p_h^n), (\mathbf{v}_h, q_h)) + \alpha \int_\Sigma (\mathbf{u}_h^n - \dot{\mathbf{d}}_h^{n-\frac{1}{2}}) \cdot \mathbf{v}_h = \int_\Sigma \boldsymbol{\lambda}_h^{n-1} \cdot \mathbf{v}_h$$

for all $(\mathbf{v}_h, q_h) \in \mathbf{V}_h^f \times M_h^f$.

3. Fluid-stress update: set $\boldsymbol{\lambda}_h^n \in \mathbf{V}_h^g$ as

$$(4.8) \quad \boldsymbol{\lambda}_h^n = \boldsymbol{\lambda}_h^{n-1} + \alpha(\dot{\mathbf{d}}_h^{n-\frac{1}{2}} - \mathbf{u}_h^n) \quad \text{on } \Sigma.$$

278

$$\mathbf{e}_{\mathbf{u},h}^n \stackrel{\text{def}}{=} \mathbf{u}_h^n - R_h^f \mathbf{u}^n, \quad e_{p,h}^n \stackrel{\text{def}}{=} p_h^n - S_h p^n, \quad \mathbf{e}_{\boldsymbol{\lambda},h}^n \stackrel{\text{def}}{=} \boldsymbol{\lambda}_h^n - \pi_h \boldsymbol{\lambda}^n,$$

279

where $\boldsymbol{\lambda}^n = \boldsymbol{\sigma}(\mathbf{u}^n, p^n) \mathbf{n}$ on the interface Σ and where R_h^f, R_h^s respectively denote the Scott-Zhang interpolants (see, e.g., [26]) projecting onto the finite element spaces \mathbf{V}_h^s and \mathbf{V}_h^f , and S_h is the Scott-Zhang interpolant into M_h^f modified by a global constant so the average on Ω^f is zero. For projecting into \mathbf{V}_h^g , we use the notation π_h , the L^2 orthogonal projection from \mathbf{V}^g to \mathbf{V}_h^g . We employ the Scott-Zhang interpolant for this analysis because it allows significant flexibility when selecting the degrees of freedom. Indeed, we may choose the degrees of freedom so that we will have $R_h^s \mathbf{v} = R_h^f \mathbf{w}$ on Σ if $\mathbf{v} \in [H^1(\Omega^s)]^2$ and $\mathbf{w} \in [H^1(\Omega^f)]^2$ and $\mathbf{v} = \mathbf{w}$ on Σ .

287

We may then define the following quantities to construct our error estimate:

288

$$\mathcal{S}_h^n \stackrel{\text{def}}{=} \|\mathbf{e}_{\mathbf{d},h}^n\|_s^2 + \rho^s \|\mathbf{e}_{\mathbf{d},h}^n\|_{0,\Omega^s}^2 + \rho^f \|\mathbf{e}_{\mathbf{u},h}^n\|_{0,\Omega^f}^2,$$

289

$$\mathcal{E}_h^n \stackrel{\text{def}}{=} \tau \alpha \|\mathbf{e}_{\mathbf{u},h}^n\|_{0,\Sigma}^2 + \frac{\tau}{\alpha} \|\mathbf{e}_{\boldsymbol{\lambda},h}^n\|_{0,\Sigma}^2,$$

290

$$\mathcal{W}_h^n \stackrel{\text{def}}{=} \rho^f \|\mathbf{e}_{\mathbf{u},h}^n - \mathbf{e}_{\mathbf{u},h}^{n-1}\|_{0,\Omega^f}^2 + 4\mu\tau \|\boldsymbol{\varepsilon}(\mathbf{e}_{\mathbf{u},h}^n)\|_{0,\Omega^f}^2 + 2\tau h^2 \|\nabla e_{p,h}^n\|_{0,\Omega^s}^2,$$

291

$$\mathcal{Z}_h^n \stackrel{\text{def}}{=} \tau \alpha \|\mathbf{e}_{\mathbf{d},h}^{n-\frac{1}{2}} - \mathbf{e}_{\mathbf{u},h}^{n-1}\|_{0,\Sigma}^2$$

292

for $1 \leq n \leq N$. Finally, as described in [13, Chapter 5], the quasi-optimal error result requires two key assumptions, which we state here. The motivation behind these assumptions will be explained further below. First, we assume that the normal \mathbf{n}^s can be extended from Σ into Ω^s in such a way that its gradient is bounded.

296

ASSUMPTION 1. *There exists $\tilde{\mathbf{n}}^s \in [\mathbf{W}^{1,\infty}(\Omega^s)]^2$ such that $\tilde{\mathbf{n}}^s|_\Sigma = \mathbf{n}^s$.*

297

The second assumption is the existence of a function $\tilde{\phi} : \Omega^s \rightarrow \mathbb{R}$ that serves as a pseudo-lifting operator from the interface Σ into the interior of the solid domain Ω^s .

299

ASSUMPTION 2. *Assume that $\tau < \frac{1}{2}$. There exists a function $\tilde{\phi} : \Omega^s \rightarrow \mathbb{R}$ satisfy-*

300 *ing:*

301 (i) $0 \leq \tilde{\phi} \leq 1$;

302 (ii) $\tilde{\phi} \in \mathbf{V}^s$;

303 (iii) $|\{x \in \Sigma : \tilde{\phi}(x) \neq 1\}| \leq C\tau$;

304 (iv) $\|\nabla \tilde{\phi}\|_{0,\Omega^s}^2 \leq C(1 + \log \frac{1}{\tau})$;

305 where each $C > 0$ represents a general constant independent of τ and of the physical
306 parameters.

307 With these assumptions established, the quasi-optimal error results proceeds as
308 follows.

309 **THEOREM 2.** *Under Assumptions 1 and 2, and assuming that the solution is*
310 *smooth enough so that Y_h defined below and $\|\varepsilon(\dot{\mathbf{d}})\|_{L^2(0,T;L^\infty(\Omega^s))}^2, \|\operatorname{div} \dot{\mathbf{d}}\|_{L^2(0,T;L^\infty(\Omega^s))}^2$*
311 *are bounded, we have the following bound on the discrete error*

$$\begin{aligned}
312 \quad (4.9) \quad & \max_{1 \leq m \leq n} \{\mathcal{S}_h^m + \mathcal{E}_h^m\} + \sum_{m=1}^n (\mathcal{Z}_h^m + \mathcal{W}_h^m) \\
313 \quad & \leq C\tau^2 \left[\frac{(1+T)(L_1+L_2)^3}{\alpha^2} \left((1 + \log \tau^{-1}) \|\varepsilon(\dot{\mathbf{d}})\|_{L^2(0,T;L^\infty(\Omega^s))}^2 \right. \right. \\
314 \quad & \left. \left. + \|\operatorname{div} \dot{\mathbf{d}}\|_{L^2(0,T;L^\infty(\Omega^s))}^2 \right) + Y_h \right],
\end{aligned}$$

315 where $Y_h \stackrel{\text{def}}{=} \sum_{i=1}^3 Y_{i,h}$ is given by

$$\begin{aligned}
316 \quad Y_{1,h} & \stackrel{\text{def}}{=} h^2 \left[(1+h^2)\rho^s(1+T)\|\partial_t \dot{\mathbf{d}}\|_{L^2(0,T;H^2(\Omega^s))}^2 + (1+h^2)\rho^f T \|\partial_t \mathbf{u}\|_{L^2(0,T;H^2(\Omega^f))}^2 \right. \\
317 \quad & + (1+T)(L_1+L_2)\|\dot{\mathbf{d}}\|_{L^2(0,T;H^2(\Omega^s))}^2 + \mu \|\mathbf{u}\|_{L^2(0,T;H^2(\Omega^f))}^2 \\
318 \quad & + \frac{h^2}{\mu} \|p\|_{L^2(0,T;H^2(\Omega^f))}^2 + (L_1+L_2)\|\mathbf{d}\|_{L^2(0,T;H^2(\Omega^s))}^2 \\
319 \quad & \left. + (L_1+L_2)\|\mathbf{d}\|_{L^\infty(0,T;H^2(\Omega^s))}^2 \right] + \tau^2 \left[\tau^2 \rho^s(1+T)\|\partial_t^3 \dot{\mathbf{d}}\|_{L^2(0,T;L^2(\Omega^s))}^2 \right. \\
320 \quad & + \rho^f T \|\partial_t^2 \mathbf{u}\|_{L^2(0,T;L^2(\Omega^f))}^2 + \frac{h^4}{\mu} \|\partial_t p\|_{L^2(0,T;H^2(\Omega^f))}^2 \\
321 \quad & \left. + h^2(L_1+L_2)\|\dot{\mathbf{d}}\|_{L^2(0,T;H^2(\Omega^s))}^2 + h^2\mu \|\partial_t \mathbf{u}\|_{L^2(0,T;H^2(\Omega^f))}^2 \right],
\end{aligned}$$

322

$$\begin{aligned}
323 \quad Y_{2,h} & \stackrel{\text{def}}{=} \tau^2 \left[(\tau^2)(1+T)(L_1+L_2)\|\partial_t^3 \dot{\mathbf{d}}\|_{L^2(0,T;H^1(\Omega^s))}^2 + h^2\|\partial_t \mathbf{u}\|_{L^2(0,T;H^3(\Omega^f))}^2 \right. \\
324 \quad & + \left(1 + \alpha + \frac{\alpha^2}{\mu} + \mu + \mu^2 + \frac{(1+T)\mu^2}{\alpha} \right) \|\partial_t \mathbf{u}\|_{L^2(0,T;H^2(\Sigma))}^2 \\
325 \quad & + (1+\alpha)\|\partial_t \dot{\mathbf{d}}\|_{L^2(0,T;L^2(\Sigma))}^2 + \left(1 + \frac{1+T}{\alpha} + \frac{1}{\mu} \right) \|\partial_t p\|_{L^2(0,T;L^2(\Sigma))}^2 \\
326 \quad & + \tau^2(1+\alpha)\|\partial_t^2 \dot{\mathbf{d}}\|_{L^2(0,T;L^2(\Sigma))}^2 + T\rho^s\|\partial_t^2 \dot{\mathbf{d}}\|_{L^2(0,T;L^2(\Omega^s))}^2 \\
327 \quad & + ((1+T)(L_1+L_2) + \rho^s)\|\partial_t \dot{\mathbf{d}}\|_{L^2(0,T;H^1(\Omega^s))}^2 + \frac{\mu^2 T}{\alpha} \|\varepsilon(\partial_t \mathbf{u})\|_{L^2(0,T;L^\infty(\Sigma))}^2
\end{aligned}$$

$$\begin{aligned}
& + \frac{T}{\alpha} \|\partial_t p\|_{L^2(0,T;L^\infty(\Sigma))}^2 + \rho^s \|\partial_t \dot{\mathbf{d}}\|_{L^\infty(0,T;L^2(\Omega^s))}^2 + h^2 \|\partial_t p\|_{L^2(0,T;H^1(\Omega^f))}^2 \\
& + h^2 (\|\mathbf{u}\|_{L^2(0,T;H^3(\Omega^f))}^2 + \|\nabla p\|_{L^2(0,T;L^2(\Omega^f))}^2) \\
& + h^4 \left(\frac{T\mu^2}{\alpha} \|\partial_t \mathbf{u}\|_{L^2(0,T;H^2(\Sigma))}^2 + \frac{T}{\alpha} \|\partial_t p\|_{L^2(0,T;H^1(\Sigma))}^2 \right), \\
Y_{3,h} & \stackrel{\text{def}}{=} \tau^2 \left[\frac{(1+T)(L_1+L_2)^3 + \rho^s(L_1^2+L_2^2)}{\alpha^2} \|\dot{\mathbf{d}}\|_{L^2(0,T;H^2(\Omega^s))}^2 \right. \\
& \left. + \frac{\rho^s T(L_1^2+L_2^2)}{\alpha^2} \|\partial_t \dot{\mathbf{d}}\|_{L^2(0,T;H^2(\Omega^s))}^2 + \frac{\rho^s(L_1^2+L_2^2)}{\alpha^2} \|\dot{\mathbf{d}}\|_{L^\infty(0,T;H^1(\Omega^s))}^2 \right].
\end{aligned}$$

4.3. Sketch of the proof to Theorem 2. The proof of Theorem 2 is only sketched below due to the page limit, we refer to [13, Theorem 5.2.9] for full details. The argument consists of three parts. First, we begin with a preliminary bound.

LEMMA 4.1. *For $1 \leq n \leq N$, it holds*

$$\frac{3}{8} \max_{1 \leq m \leq n} \{S_h^m + \mathcal{E}_h^m\} + \frac{3}{8} \sum_{m=1}^n (\mathcal{W}_h^m + \mathcal{Z}_h^m) \leq \sum_{m=1}^n \frac{\tau}{\alpha} \int_{\Sigma} e_{\lambda,h}^{m-1} \cdot \mathbf{g}_{3,h}^m + CD_h^n,$$

where

$$\mathbf{g}_{3,h}^n \stackrel{\text{def}}{=} \frac{\alpha}{2} \mathbf{g}_{1,h}^n + \pi_h \mathbf{g}_2^n, \quad \mathbf{g}_{1,h}^n \stackrel{\text{def}}{=} R_h^f \mathbf{u}^n - R_h^f \mathbf{u}^{n-1}, \quad \mathbf{g}_2^n \stackrel{\text{def}}{=} \boldsymbol{\lambda}^n - \boldsymbol{\lambda}^{n-1}$$

and

$$\begin{aligned}
D_h^n & \stackrel{\text{def}}{=} \tau \sum_{m=1}^{n-1} \left[\mu \|\varepsilon((R_h^f - I)\mathbf{u}^m)\|_{0,\Omega^f}^2 + \frac{1}{\mu} \|(S_h - I)p^m\|_{0,\Omega^f}^2 \right. \\
& + (1+T) \|R_h^s \dot{\mathbf{d}}^{m-\frac{1}{2}} - \partial_\tau R_h^s \mathbf{d}_h^m\|_s^2 + (1+T) \|(R_h^s - I) \partial_\tau \mathbf{d}^m\|_s^2 + h^2 \|\mathbf{u}^m\|_{H^3(\Omega^f)}^2 \\
& + (1+T) \|R_h^s \dot{\mathbf{d}}^{m-\frac{1}{2}} - \partial_\tau R_h^s \mathbf{d}_h^m\|_s^2 + (1+T) \|(R_h^s - I) \partial_\tau \mathbf{d}^m\|_s^2 + h^2 \|\mathbf{u}^m\|_{3,\Omega^f}^2 \\
& + \left(\alpha + \frac{\alpha^2}{\mu} \right) \|\mathbf{g}_{1,h}^m\|_{0,\Sigma}^2 + \left(1 + \frac{1}{\alpha} + \frac{1}{\mu} \right) \|\boldsymbol{\lambda}^m - \boldsymbol{\lambda}^{m-1}\|_{0,\Sigma}^2 \\
& + T \rho^s \|\partial_\tau R_h^s \dot{\mathbf{d}}^m - \partial_t \dot{\mathbf{d}}^{m-\frac{1}{2}}\|_{0,\Omega^s}^2 + \rho^f T \|\partial_\tau R_h^f \mathbf{u}^m - \partial_t \mathbf{u}^m\|_{0,\Omega^f}^2 \\
& \left. + h^2 \|\nabla S_h p^m\|_{0,\Omega^f}^2 + \frac{\tau}{2\alpha} \|\mathbf{g}_{3,h}^m\|_{0,\Sigma}^2 \right] + \|(R_h^s - I)\mathbf{d}^m\|_s^2.
\end{aligned}$$

The proof of Lemma 4.1 requires some standard algebra along with Cauchy-Schwarz, Young's inequality, trace inequality, and Korn's inequality. A detailed proof is included in [13, Chapter 5]. The key takeaway, however, is that all of the terms in D_h^n are either the norms of splitting error terms such as $\mathbf{g}_{1,h}^n$ or interpolation errors such as $S_h p^n - p^n$. In both cases, the terms may be optimally bounded in terms of h and τ in the final step of the proof. However, the remaining unbounded term requires special care.

Consequently, the second part of the proof involves deriving a bound for the term

$$\sum_{m=1}^n \frac{\tau}{\alpha} \int_{\Sigma} e_{\lambda,h}^{m-1} \cdot \mathbf{g}_{3,h}^m.$$

351 If we attempt to bound this term by balancing $e_{\lambda,h}^{m-1}$ with terms appearing on the
 352 left-hand side of the estimate, we ultimately sacrifice a factor of $\tau^{\frac{1}{2}}$, resulting in
 353 suboptimal convergence, as done in [6]. Essentially, the challenge presented by this
 354 term is that it resides on the interface Σ , but to avoid a loss in accuracy we must
 355 somehow avoid the interface as much as possible.

356 To do this, we utilize the error equations of the solid to pull the term $e_{\lambda,h}^{n-1}$ from
 357 the interface Σ into the interior domain Ω^s . However, this requires us to construct
 358 an extension of $\mathbf{g}_{3,h}^n$ into Ω^s which is in \mathbf{V}_h^s . Critically, this means that the extension
 359 needs to vanish on $\partial\Omega^s \setminus \Sigma$, which is not guaranteed for $\mathbf{g}_{3,h}^{n+1}$ due to the presence of
 360 the term $\pi_h(\boldsymbol{\lambda}^{n+1} - \boldsymbol{\lambda}^n)$. Therefore, we will utilize the extended normal $\tilde{\mathbf{n}}_s$ and the
 361 function $\tilde{\phi}$ defined in Assumptions 1 and 2 to construct a cut-off function technique
 362 to continuously lift the residual $\mathbf{g}_{3,h}^{n+1}$ from \mathbf{V}_h^s into \mathbf{V}_h^s .

363 The result of this extension step yields a quasi-optimal bound stated in the fol-
 364 lowing lemma.

LEMMA 4.2. *Under Assumptions 1 and 2 we have*

$$\frac{\tau}{\alpha} \sum_{m=1}^n \int_{\Sigma} e_{\lambda,h}^{m-1} \cdot \mathbf{g}_{3,h}^m \leq \frac{1}{8} \max_{1 \leq m \leq n} \{ \mathcal{S}_h^m + \mathcal{E}_h^m \} + \frac{1}{8} \sum_{m=1}^n \mathcal{Z}_h^m + C\Psi_h^n,$$

365 where $\Psi_h^n \stackrel{\text{def}}{=} \Psi_{1,h}^n + \Psi_{2,h}^n$ given by

$$\begin{aligned} 366 \quad \Psi_1^n &\stackrel{\text{def}}{=} T\tau^3 \rho^s \sum_{m=1}^n \|\partial_\tau^2 R_h^s \dot{\mathbf{d}}^m\|_{0,\Omega^s}^2 + \rho^s \|\mathbf{g}_{1,h}^n\|_{0,\Omega^s}^2 \\ 367 \quad &+ \tau \sum_{m=1}^m \left[(1+T) \|\mathbf{g}_{1,h}^m\|_s^2 + (1+\alpha) \|\mathbf{g}_{1,h}^m\|_{0,\Sigma}^2 + \|\boldsymbol{\lambda}^m - \boldsymbol{\lambda}^{m-1}\|_{0,\Sigma}^2 \right. \\ 368 \quad &+ \rho^s \|\partial_\tau R_h^s \dot{\mathbf{d}}^m - \partial_t \dot{\mathbf{d}}^{m-\frac{1}{2}}\|_{0,\Omega^s}^2 + \rho^s \|\mathbf{g}_{1,h}^{n+1}\|_{0,\Omega^s}^2 + \|(R_h^s - I)\mathbf{d}^{m-\frac{1}{2}}\|_s^2 \\ 369 \quad &+ \alpha \|R_h^s \mathbf{u}^m - \partial_\tau R_h^s \mathbf{d}^m\|_{0,\Sigma}^2 + \alpha \|R_h^s \dot{\mathbf{d}}^{m-\frac{1}{2}} - \partial_\tau R_h^s \mathbf{d}_h^m\|_{0,\Sigma}^2 \left. \right], \end{aligned}$$

370

$$\begin{aligned} 371 \quad \Psi_2^n &\stackrel{\text{def}}{=} \frac{T\tau^3 \rho^s}{\alpha^2} \sum_{m=1}^n \|\partial_\tau^2 R_h^s (\tilde{\phi} \boldsymbol{\sigma}(\mathbf{d}^{m-1}) \tilde{\mathbf{n}}^s)\|_{0,\Omega^s}^2 + \frac{\rho^s}{\alpha^2} \|\tilde{\mathbf{g}}_{2,h}^n\|_{0,\Omega^s}^2 + \frac{Th^2}{\alpha} \sum_{m=1}^n \|\mathbf{g}_2^m\|_{1,\Sigma}^2 \\ 372 \quad &+ \tau \sum_{m=1}^n \left[\frac{1+T}{\alpha^2} \|\tilde{\mathbf{g}}_{2,h}^m\|_s^2 + (1+\frac{1}{\alpha}) \|\boldsymbol{\lambda}^{n+1} - \boldsymbol{\lambda}^n\|_{0,\Sigma}^2 \right. \\ 373 \quad &+ \|\mathbf{g}_{1,h}^m\|_{0,\Sigma}^2 + \rho^s \|\partial_\tau R_h^s \dot{\mathbf{d}}^m - \partial_t \dot{\mathbf{d}}^{m-\frac{1}{2}}\|_{0,\Omega^s}^2 + \frac{\rho^s}{\alpha^2} \|\tilde{\mathbf{g}}_{2,h}^m\|_{0,\Omega^s}^2 \\ 374 \quad &+ \|(R_h^s - I)\mathbf{d}^{m-\frac{1}{2}}\|_s^2 + \|R_h^s \mathbf{u}^m - \partial_\tau R_h^s \mathbf{d}^m\|_{0,\Sigma}^2 \\ 375 \quad &+ \|R_h^s \dot{\mathbf{d}}^{m-\frac{1}{2}} - \partial_\tau R_h^s \mathbf{d}_h^m\|_{0,\Sigma}^2 + \frac{T}{\alpha} \|\mathbf{g}_2^m\|_{L^\infty(\Sigma)}^2 \left. \right]. \end{aligned}$$

376 Finally, in the third step of the proof, it remains to bound the terms D_h^n and Ψ_h^n ,
 377 which is the purpose of the next lemma.

378 LEMMA 4.3. *Under Assumptions 1 and 2, we have, for $1 \leq n \leq N$,*

$$D_h^n + \Psi_h^n \leq C\tau^2 \left[\frac{(1+T)(L_1+L_2)^3}{\alpha^2} \left((1+\log \tau^{-1}) \|\boldsymbol{\varepsilon}(\dot{\mathbf{d}})\|_{L^2(0,T;L^\infty(\Omega^s))}^2 + \|\operatorname{div} \dot{\mathbf{d}}\|_{L^2(0,T;L^\infty(\Omega^s))}^2 \right) + CY_h \right].$$

The error estimate (4.9) then follows by combining the results of Lemmas 4.1–4.3.

5. Numerical examples. In this section, we illustrate the accuracy properties of Algorithms 3.1 in a series of well-known numerical examples.

5.1. Convergence study in a simplified framework. The objective of this first example is to provide numerical evidence of the nearly-optimal convergence result of Theorem 2. We will in particular investigate the effect on the accuracy of the solid parameters L_1, L_2 involved in the error estimate (4.9). To this purpose, we consider the pressure wave propagation benchmark of [18, Section 6.1.1] with the simplified coupled problem (4.1)–(4.3). We hence take $\Omega^f = [0, L] \times [0, R]$, $\Omega^s = [0, L] \times [R, R+\epsilon]$, with $L = 6$, $R = 0.5$ and $\epsilon = 0.1$. All the units are in the CGS system. At the fluid inlet boundary $x = 0$ a sinusoidal pressure of maximal amplitude $2 \cdot 10^4$ is enforced during $5 \cdot 10^{-3}$ second. Zero traction is prescribed at the outlet $x = 6$ and a symmetry condition is enforced on the lower wall. Transverse membrane effects are included in the solid equation (4.2)₁ through the additional zeroth-order term $c_0 \mathbf{d}$. The solid is clamped at its extremities and zero traction is enforced on its top boundary.

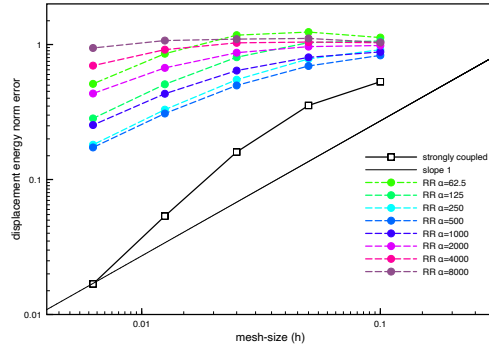


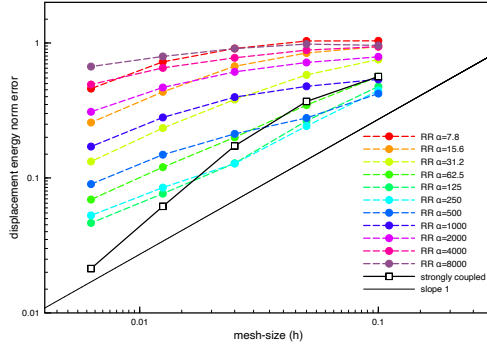
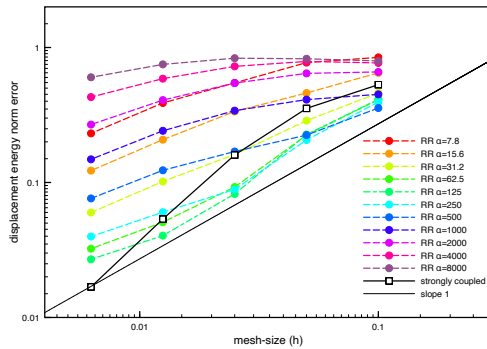
FIG. 1. *Convergence histories for $E = 1.58 \cdot 10^6$.*

The fluid and solid physical parameters are $\rho^f = 1$, $\mu = 0.035$, $\rho^s = 1.1$, $L_1 = 1.15 \cdot 10^6$, $L_2 = 1.7 \cdot 10^6$ and $c_0 = 4 \cdot 10^6$. The pressure stabilization parameter in (4.5) is set to $\gamma_p = 10^{-3}$. All the computations have been carried out with the **FreeFem++** software (see [25]).

In order to illustrate the accuracy of Algorithm 4.1, we evaluate the relative displacement error $\|\mathbf{d}_h^N - \mathbf{d}(T)\|_e / \|\mathbf{d}(T)\|_e$ at the final time $T = 0.015$ for different values of the discretization parameters under $\tau = \mathcal{O}(h)$, namely,

$$\tau \in \{5 \cdot 10^{-4} / 2^i\}_{i=0}^4, \quad h \in \{0.1 / 2^i\}_{i=0}^4.$$

The relative errors are calculated with a reference solution obtained with an implicit coupling scheme and a fine space-time grid ($h = 0.003125$ and $\tau = 10^{-6}$). The resulting convergence histories are reported in Figures 1–3 for three decreasing values


 FIG. 2. *Convergence histories for $E = 3.16 \cdot 10^5$.*

 FIG. 3. *Convergence histories for $E = 1.58 \cdot 10^5$.*

403 of the Young modulus E . For comparison purposes, the results obtained with the
 404 implicit coupling scheme are also provided.

405 Several remarks are in order. The results indicate that there exists an optimal
 406 value of the Robin parameter α in terms of accuracy, and that accuracy tends to
 407 degrade for large or small values of α . Figures 1–3 also show that overall first-order
 408 accuracy $\mathcal{O}(h)$ is obtained for some values of α . This is more noticeable in Figures 2
 409 and 3. The results show that accuracy tends to degrade when increasing the elastic
 410 parameters L_1 and L_2 . All these observations are in agreement with the error estimate
 411 provided by Theorem 2. The results of Figures 1–3 indicate also that the optimal
 412 value of the Robin parameter α is proportional to \sqrt{E} . Such scaling equilibrates the
 413 contributions of the error bound provided by Theorem 2, which suggests the choice
 414 $\alpha = \gamma\sqrt{\rho^s E}$, with γ a user-defined dimensionless parameter.

415 **5.2. Lid-driven cavity with flexible bottom.** As second numerical example,
 416 we consider the classical shear-driven cavity problem with a flexible bottom (see, e.g.,
 417 [20]). The fluid domain is the unit square $\Omega^f = [0, 1] \times [0, 1]$ with the fluid-solid
 418 interface on the lower boundary $\Sigma = [0, 1] \times \{0\}$. All the units are given in the SI
 419 system.

420 The system is described by the non-linear coupled problem (2.1)-(2.3) in which
 421 the solid model (2.2) is replaced by a non-linear Timoshenko beam (see, e.g., [3]). The
 422 overall system is initially at rest and an oscillating shear velocity profile is imposed on
 423 the upper boundary $\mathbf{u}(t) = (1 - \cos(0.4\pi t), 0)^T$ on $[0, 1] \times \{1\}$. A no-slip condition is

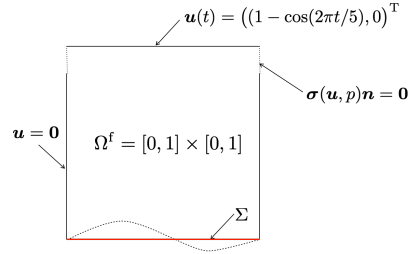
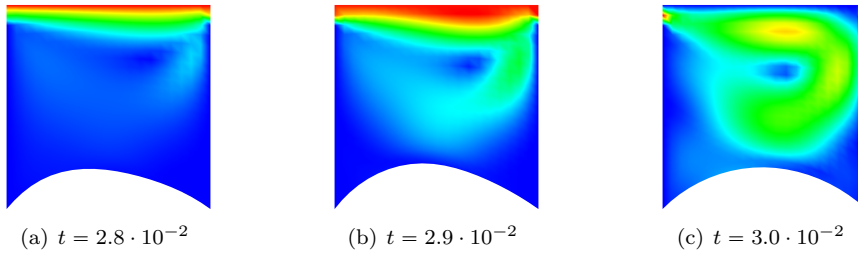
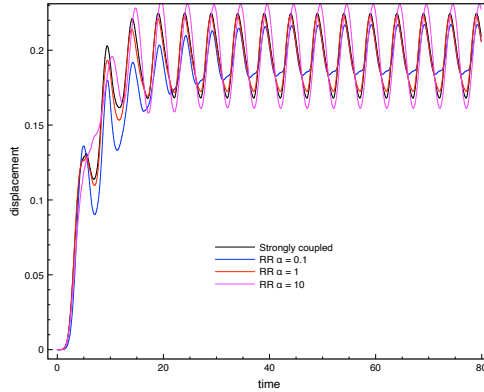


FIG. 4. Geometric description.

FIG. 5. Snapshots of the fluid velocity in the deformed configuration at three different time instants obtained with Algorithm 3.1 and $\alpha = 1$.FIG. 6. Time history of the mid-point displacement magnitude obtained with Algorithm 3.1, for three different values of α , and a strongly coupled scheme.

424 enforced on the portions $\{0, 1\} \times [0, 0.9]$ of the lateral cavity walls, and zero traction
 425 is prescribed on the remaining parts $\{0, 1\} \times [0.9, 1]$. The fluid physical parameters are
 426 given by $\rho^f = 1.0$ and $\mu = 0.01$, and for the solid $\rho^s = 250$, $\epsilon = 0.002$, $E = 250$ and
 427 $\nu = 0$.

428 The spatial fluid approximation in (3.11) is made of Q_1/Q_1 finite elements with
 429 a SUPG/PSPG stabilized formulation. Linear MITC beam elements are used for the
 430 approximation of the Timoshenko beam in (3.10). In this numerical example, the
 431 computational meshes for the fluid and the solid meshes are, respectively, made of
 432 400 quadrilaterals and of 20 segments and a time-step length of $\tau = 0.1$ is considered.

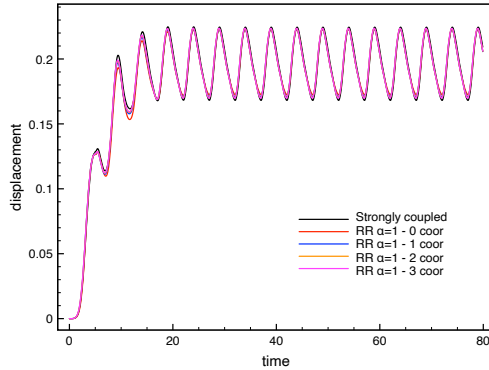


FIG. 7. Time history of the interface mid-point displacement magnitude obtained with Algorithm 3.1, for $\alpha = 1$ and different correction iterations, and a strongly coupled scheme.

433 All the numerical computations have been performed with the FELiScE library¹.

434 For illustration purposes, we have reported in Figure 5 some snapshots of the fluid
 435 velocity magnitude in the current configuration at different time-instants, obtained
 436 with Algorithm 3.1 and $\alpha = 1$. We now focus on the accuracy of this loosely coupled
 437 scheme. To this purpose, we have first reported in Figure 6 the magnitude of the
 438 interfacial mid-point displacement obtained with Algorithm 3.1, for different values
 439 of α , and with a strongly coupled scheme. The impact of α on the accuracy is
 440 clearly visible. As in the previous numerical example (Section 5.1), the accuracy of
 441 Algorithm 3.1 degrades when α is both smaller and larger than the optimal value
 442 (here, around $\alpha = 1$). It is also worth noting the very good accuracy of the results
 443 obtained with Algorithm 3.1 and $\alpha = 1$. Indeed, without any correction iteration
 444 the proposed loosely coupled scheme delivers practically the same accuracy as the
 445 strongly coupled scheme. This observation is in line with the results of the previous
 446 section (Figures 1–3) and the error estimate of Theorem 2, which indicate that small
 447 values of the solid elastic parameters yield a low splitting error.

448 Finally, Figure 7 compares the results obtained with Algorithm 3.1 for $\alpha = 1$ and
 449 different correction iterations. We recall that one correction iteration corresponds to
 450 performing once more steps (3.10), (3.11) and (3.12) of Algorithm 3.1 with updated
 451 Robin conditions, that is, by initializing $\boldsymbol{\lambda}^{n-1}$ and $\hat{\mathbf{u}}^{n-1}|_{\Sigma}$ with the last values of $\boldsymbol{\lambda}^n$
 452 and $\hat{\mathbf{u}}^n|_{\Sigma}$. Since the accuracy is already very good without any correction, it only
 453 slight improves as we increase the number of corrections.

454 **5.3. Pressure wave in an elastic tube.** We consider the 3D non-linear counter-
 455 part of the numerical example considered in Section 5.1, viz., the propagation of a
 456 pressure wave within an elastic tube (see, e.g., [19, Chapter 12]). The fluid domain is
 457 a straight tube of radius 0.5 and length 5. The vessel wall has a thickness of 0.1. All
 458 the units are given in the CGS system. The fluid-structure system is modeled by the
 459 non-linear coupled problem (2.1)-(2.3). The overall system is initially at rest and an
 460 over pressure of $1.3332 \cdot 10^4$ is imposed on the inlet boundary during the time interval
 461 $[0, 0.005]$. The solid wall is clamped at its extremities. The physical parameters for
 462 the fluid are $\rho^f = 1$ and $\mu = 0.035$, and for the solid $\rho^s = 1.2$, $E = 3 \cdot 10^6$ and $\nu = 0.3$.
 463 In (3.10) and (3.11) continuous \mathbb{P}_1 finite elements are used (a SUPG/PSPG stabilized
 464 formulation is considered in the fluid). All the numerical computations have been

¹<https://gitlab.inria.fr/felisce/felisce>

465 performed with the FELiScE library.

466 To highlight the fluid-structure interaction in this numerical example, Figure 8
 467 shows snapshots of the fluid pressure in the deformed configuration at different time-
 instants, obtained using Algorithm 3.1 with $\alpha = 500$. We will now assess the influence

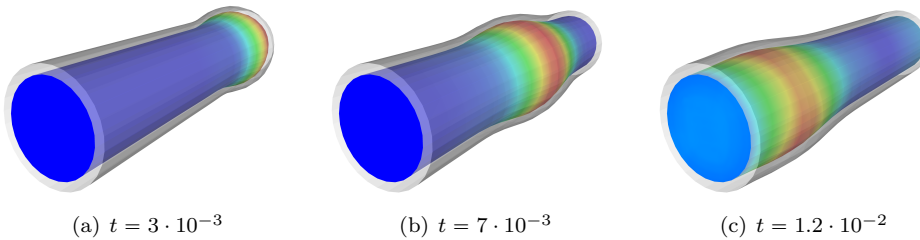


FIG. 8. Snapshots of the fluid pressure in the deformed configuration at three different time instants with $\alpha = 500$.

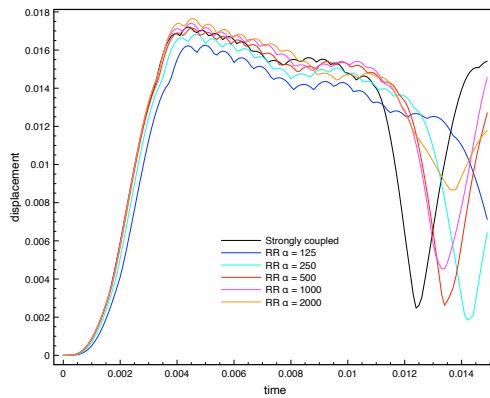


FIG. 9. Time history of the interface mid-point displacement magnitudes with implicit coupling and RR algorithm with different α .

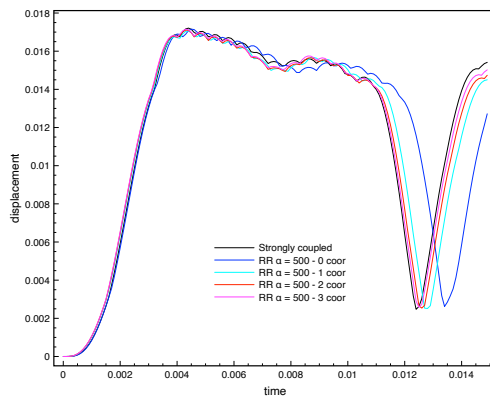


FIG. 10. Time history of the interface mid-point displacement magnitudes with implicit coupling and RR algorithm with $\alpha = 500$ and different corrections.

469 of the parameter α . In Figure 9, we display the magnitude of the interfacial mid-point
 470 displacement calculated using Algorithm 3.1 for various α values. These results are
 471 then compared to those obtained using a strongly coupled scheme. As observed in the
 472 previous numerical examples, the performance of Algorithm 3.1 is closely linked to the
 473 choice of α . Specifically, Algorithm 3.1 shows good accuracy when α is approximately
 474 500. However, as we deviate from this range, both smaller and larger values of α tend
 475 to degrade the accuracy.

476 Figure 10 illustrates the impact of some correction iterations in Algorithm 3.1
 477 with $\alpha = 500$. We observe an improvement in the accuracy of Algorithm 3.1 as
 478 we increase the number of corrections. It is worth noting that a single iteration
 479 significantly improves the accuracy. Large values of the solid physical parameters can
 480 negatively impact the solution, necessitating correction iterations to achieve accurate
 481 results.

482 **6. Conclusion.** We have extended the stability results of the loosely coupled
 483 Robin-Robin coupling from [6] to the fully nonlinear case. A nearly-optimal error
 484 estimate was also reported for the linear case. The numerical section validated the
 485 theoretical results, but also pointed to the importance of making a judicious choice
 486 of the Robin parameter α in order to observe optimal convergence in the range of
 487 discretization parameters used.

488

REFERENCES

- 489 [1] S. BADIA, F. NOBILE, AND C. VERGARA, *Robin-Robin preconditioned Krylov methods for*
 490 *fluid-structure interaction problems*, *Comput. Methods Appl. Mech. Engrg.*, 198 (2009),
 491 pp. 2768–2784, [https://doi.org/10.1016/j.cma.](https://doi.org/10.1016/j.cma.2009.04.004)
 492 [2009.04.004](https://doi.org/10.1016/j.cma.2009.04.004).
- 493 [2] J. W. BANKS, W. D. HENSHAW, AND D. W. SCHWENDEMAN, *An analysis of a new stable*
 494 *partitioned algorithm for FSI problems. Part I: Incompressible flow and elastic solids*, *J.*
 495 *Comput. Phys.*, 269 (2014), pp. 108–137, <https://doi.org/10.1016/j.jcp.2014.03.006>, <https://doi.org/10.1016/j.jcp.2014.03.006>.
- 497 [3] K. BATHE, *Finite Element Procedures*, Prentice Hall, 1996.
- 498 [4] F. BREZZI AND J. PITKÄRANTA, *On the stabilization of finite element approximations of the*
 499 *Stokes equations*, in *Efficient solutions of elliptic systems* (Kiel, 1984), vol. 10 of *Notes*
 500 *Numer. Fluid Mech.*, Vieweg, 1984, pp. 11–19.
- 501 [5] M. BUKAČ, S. ČANIĆ, R. GLOWINSKI, B. MUHA, AND A. QUAINI, *A modular, operator-splitting*
 502 *scheme for fluid-structure interaction problems with thick structures*, *Internat. J. Numer.*
 503 *Methods Fluids*, 74 (2014), pp. 577–604, <https://doi.org/10.1002/fld.3863>, <https://doi.org/10.1002/fld.3863>.
- 505 [6] E. BURMAN, R. DURST, M. FERNÁNDEZ, AND J. GUZMÁN, *Fully discrete loosely coupled Robin-*
 506 *Robin scheme for incompressible fluid-structure interaction: stability and error analy-*
 507 *sis*, *Numer. Math.*, 151 (2022), pp. 807–840, <https://doi.org/10.1007/s00211-022-01295-y>,
 508 <https://doi.org/10.1007/s00211-022-01295-y>.
- 509 [7] E. BURMAN, R. DURST, M. FERNÁNDEZ, AND J. GUZMÁN, *Loosely coupled, non-iterative time-*
 510 *splitting scheme based on Robin-Robin coupling: unified analysis for parabolic/parabolic*
 511 *and parabolic/hyperbolic problems*, *J. Numer. Math.*, 31 (2023), pp. 59–77, <https://doi.org/10.1515/jnma-2021-0119>, <https://doi.org/10.1515/jnma-2021-0119>.
- 513 [8] E. BURMAN, R. DURST, AND J. GUZMÁN, *Stability and error analysis of a splitting method using*
 514 *Robin-Robin coupling applied to a fluid-structure interaction problem*, *Numer. Methods*
 515 *Partial Differential Equations*, 38 (2022), pp. 1396–1406, [https://doi.org/10.1002/num.](https://doi.org/10.1002/num.22840)
 516 [22840](https://doi.org/10.1002/num.22840), <https://doi.org/10.1002/num.22840>.
- 517 [9] E. BURMAN AND M. FERNÁNDEZ, *Stabilization of explicit coupling in fluid-structure interac-*
 518 *tion involving fluid incompressibility*, *Comput. Methods Appl. Mech. Engrg.*, 198 (2009),
 519 pp. 766–784, <https://doi.org/10.1016/j.cma.2008.10.012>, [https://doi.org/10.1016/j.cma.](https://doi.org/10.1016/j.cma.2008.10.012)
 520 [2008.10.012](https://doi.org/10.1016/j.cma.2008.10.012).
- 521 [10] E. BURMAN AND M. FERNÁNDEZ, *Explicit strategies for incompressible fluid-structure inter-*
 522 *action problems: Nitsche type mortaring versus Robin-Robin coupling*, *Internat. J. Nu-*

- mer. Methods Engrg., 97 (2014), pp. 739–758, <https://doi.org/10.1002/nme.4607>, <https://doi.org/10.1002/nme.4607>.
- [11] E. BURMAN, M. FERNÁNDEZ, AND P. HANSBO, *Continuous interior penalty finite element method for Oseen’s equations*, SIAM J. Numer. Anal., 44 (2006), pp. 1248–1274.
- [12] P. CAUSIN, J. F. GERBEAU, AND F. NOBILE, *Added-mass effect in the design of partitioned algorithms for fluid-structure problems*, Comput. Methods Appl. Mech. Engrg., 194 (2005), pp. 4506–4527, <https://doi.org/10.1016/j.cma.2004.12.005>, <https://doi.org/10.1016/j.cma.2004.12.005>.
- [13] R. DURST, *Recent Advances in Splitting Methods Based on Robin-Robin Coupling Conditions*, PhD thesis, Brown University, 2022, <https://repository.library.brown.edu/studio/item/bdr:v34deskr/>.
- [14] C. FARHAT, P. GEUZAINÉ, AND C. GRANDMONT, *The discrete geometric conservation law and the nonlinear stability of ale schemes for the solution of flow problems on moving grids*, Journal of Computational Physics, 174 (2001), pp. 669–694.
- [15] C. FARHAT, M. LESOINNE, AND P. LETALLEC, *Load and motion transfer algorithms for fluid/structure interaction problems with non-matching discrete interfaces: momentum and energy conservation, optimal discretization and application to aeroelasticity*, Comput. Methods Appl. Mech. Engrg., 157 (1998), pp. 95–114, [https://doi.org/10.1016/S0045-7825\(97\)00216-8](https://doi.org/10.1016/S0045-7825(97)00216-8), [https://doi.org/10.1016/S0045-7825\(97\)00216-8](https://doi.org/10.1016/S0045-7825(97)00216-8).
- [16] M. FERNÁNDEZ AND J.-F. GERBEAU, *Algorithms for fluid-structure interaction problems*, in Cardiovascular mathematics, vol. 1 of MS&A. Model. Simul. Appl., Springer, 2009, pp. 307–346.
- [17] M. FERNÁNDEZ AND J. MULLAERT, *Convergence and error analysis for a class of splitting schemes in incompressible fluid-structure interaction*, IMA J. Numer. Anal., 36 (2016), pp. 1748–1782, <https://doi.org/10.1093/imanum/drv055>, <https://doi.org/10.1093/imanum/drv055>.
- [18] M. FERNÁNDEZ, J. MULLAERT, AND M. VIDRASCU, *Generalized Robin-Neumann explicit coupling schemes for incompressible fluid-structure interaction: stability analysis and numerics*, Internat. J. Numer. Methods Engrg., 101 (2015), pp. 199–229.
- [19] L. FORMAGGIA, A. QUARTERONI, AND A. VENEZIANI, eds., *Cardiovascular Mathematics. Modeling and simulation of the circulatory system*, vol. 1 of Modeling, Simulation and Applications, Springer, 2009.
- [20] C. FÖRSTER, W. WALL, AND E. RAMM, *Artificial added mass instabilities in sequential staggered coupling of nonlinear structures and incompressible viscous flows*, Comput. Methods Appl. Mech. Engrg., 196 (2007), pp. 1278–1293.
- [21] G. GIGANTE AND C. VERGARA, *On the stability of a loosely-coupled scheme based on a Robin interface condition for fluid-structure interaction*, Comput. Math. Appl., 96 (2021), pp. 109–119, <https://doi.org/10.1016/j.camwa.2021.05.012>, <https://doi.org/10.1016/j.camwa.2021.05.012>.
- [22] G. GIGANTE AND C. VERGARA, *On the stability of a loosely-coupled scheme based on a Robin interface condition for fluid-structure interaction*, Comput. Math. Appl., 96 (2021), pp. 109–119, <https://doi.org/10.1016/j.camwa.2021.05.012>, <https://doi.org/10.1016/j.camwa.2021.05.012>.
- [23] O. GONZALEZ, *Exact energy and momentum conserving algorithms for general models in nonlinear elasticity*, Computer Methods in Applied Mechanics and Engineering, 190 (2000), pp. 1763–1783.
- [24] P. HANSBO, J. HERMANSSON, AND T. SVEDBERG, *Nitsche’s method combined with space-time finite elements for ALE fluid-structure interaction problems*, Comput. Methods Appl. Mech. Engrg., 193 (2004), pp. 4195–4206, <https://doi.org/10.1016/j.cma.2003.09.029>, <https://doi.org/10.1016/j.cma.2003.09.029>.
- [25] F. HECHT, *New development in FreeFem++*, J. Numer. Math., 20 (2012), pp. 251–265.
- [26] L. SCOTT AND S. ZHANG, *Finite element interpolation of nonsmooth functions satisfying boundary conditions*, Mathematics of Computation, 54 (1990), pp. 483–493.
- [27] A. SEBOLDT AND M. BUKAČ, *A non-iterative domain decomposition method for the interaction between a fluid and a thick structure*, Numer. Methods Partial Differential Equations, 37 (2021), pp. 2803–2832.
- [28] S. SMALDONE, *Numerical analysis and simulations of coupled problems for the cardiovascular system*, PhD thesis, Université Pierre et Marie Curie, 2014. <https://tel.archives-ouvertes.fr/tel-01287506>.
- [29] T. TEZDUYAR, *Stabilized finite element formulations for incompressible flow computations*, vol. 28 of Advances in Applied Mechanics, Elsevier, 1991, pp. 1–44, [https://doi.org/https://doi.org/10.1016/S0065-2156\(08\)70153-4](https://doi.org/https://doi.org/10.1016/S0065-2156(08)70153-4).